Main research topic: Marine Structural Mechanics

Title: Friction models for evaluating dynamic stresses in non-bonded flexible risers

Authors: Tianjiao Dai, Svein Sævik, Naiquan Ye

Abstract
This paper addresses friction models used for evaluating dynamic stresses in non-bonded flexible risers. A review of the most commonly used methods to model friction between layers in such structures was performed. Four models for calculating friction under dynamic contact pressure and constant shear interaction stick stiffness conditions were then formulated to enable stress calculation of cross-sections exposed to variable tension and bending loads. The friction models were implemented into a computer code used for numerical studies. A sensitivity study was carried out to determine the optimum shear interaction stick stiffness parameter, K_0, with respect to representing the plane surfaces remain plane assumption. This was followed by an investigation of the performance of the developed models with respect to the tendon axial force next to the outermost fibre position. The proposed friction models were also verified against full scale tests in terms of bending moment-curvature data. As the test data indicated less bending stiffness in the stick domain than that can be obtained by the plane surfaces remain plane assumption, a method to estimate the parameter K_0 was proposed, which accounted for the shear deformation of the plastic layers. The initial strain concept was further applied to deal with the significant hysteresis observed in the test data for low internal pressures pointing the way forward with respect to dealing with this effect in stress analysis. Furthermore, a friction model comparison study was carried out for investigating the static friction effect on the axial force at the outermost fibre position and the bending moment-curvature relationship.

1. Introduction

The flexible riser concept may be applied for flexible pipes, power cables and umbilicals. All consist of several layers involving various materials and components in the composite cross-section, which depend on the specific application. In general, flexible pipes are used to transport oil and gas, whereas umbilicals may serve different purposes such as chemical injection, electrical and hydraulic power transmissions/control and monitoring. The umbilical cross-section may therefore include steel tubes, tensile armors, fluid conduits, electrical cables and fibre optic cables. As the fatigue performance of the cross-section components always determines the fatigue life of the whole structure for dynamic applications, it is of great importance to correctly predict the dynamic stresses in each cross-section element.

The most important stress component with respect to fatigue is the helix element's longitudinal stress caused by tension and bending variations. The longitudinal stress includes contribution from axial force and local bending, where friction in many cases governs the axial force variation. Many researchers have emphasized the importance of including all stress contributions in the local stress analysis to obtain correct fatigue life, see [1, 2, 3, 4, 5]. Therefore, accurate modeling of the friction stress behavior becomes important in fatigue design. There are various strategies to deal with friction in such structures. The ideal method would be to model the complex cross-section by full 3D approaches, however resulting in long computing time. Therefore, the global response and local stress analyses are normally separated. The curvature and tension time histories from the global analysis are used as input to generate the helical elements' stress history from local analysis. These local analyses are usually performed at selected locations, i.e., the hang-off, sagging, hogging, and touch down sections of a flexible riser. The local analysis can be achieved by analytical methods or finite element approaches.

Most analytical and 2D finite element approaches are feasible only if the stress state is fully determined by the global quantities at the selected cross-section, e.g., tension and curvature, which requires that 3D effects are negligible. The moment-curvature relation established from the 2D model can also be implemented into 3D-beam element material models to capture the hysteresis effect during global dynamic time domain analysis. Then the stress history can be found from post-processing directly. Otherwise, 3D approaches based on modeling each helix individually over a sufficient model length are needed. This requires a shear interaction formulation describing layer contact in combination with a stick-slip model for friction which is the focus in the present paper. The slip between adjacent layers occurs if the maximum static friction force is exceeded by the shear force induced by bending loads. Typically, the complex cross-section structure behaves like a rigid pipe before slip, whereas after slip, the friction force becomes constant. Some models, e.g., as proposed by Sævik [6], are based on an elastic-plastic friction model where the maximum elastic relative deformation is determined by a fixed stick displacement which means that the shear interaction stick stiffness represented by the parameter, K_0, may be too small to obtain the assumption of plane surfaces remain plane at small contact pressures. Therefore, a constant K_0 approach is applied in the present work.

When it comes to the importance of the friction coefficient, Kavanagh et al. [1] established two non-linear time domain models using respective no friction and full friction, giving a factor 10 difference in fatigue life. In Olsen et al.'s work [7], friction tests for different materials in an umbilical were reported. A reduction from 0.25 to 0.2 in the friction coefficient resulted in a factor 2 larger fatigue life, demonstrating the importance of the friction coefficient.

The friction coefficient in shear interaction models is normally measured by testing, obtained as an average value between the static and dynamic friction coefficients observed during cyclic runs. More importantly, static and dynamic friction coefficients and the corresponding smooth transition between these two friction coefficients were observed by Rabinowicz [8] in some tests. Several works have been reported in the literature, see [3, 9, 10, 11, 12, 13], concerning the hysteric bending behavior of helix elements versus full scale tests. Most of the work demonstrated that good correlation in terms of axial stress of helix elements and hysteresis bending moment-curvature relationship. However, none of these works considered the interaction

between static and dynamic friction during the alternating slip process. Therefore, it is of interest to develop a static friction model that includes both static and dynamic friction effects and investigate the consequence of such behavior in a complex cross-section.

Dynamic tests for investigation of internal friction were carried out at Marintek in 1991, as reported by Skallerud [14]. In these tests, a pronounced hysteresis was found in the bending moment-curvature relationship even for small internal pressure levels (small true wall tension). One way of explaining this phenomenon is that contact pressures exist between the layers in the initial state due to material shrinking of the outer sheath resulting from the manufacturing process. As of today, standard industry practice is to neglect this contribution. The initial strain concept is therefore proposed as a method for reproducing the results seen in the test measurements, thus pointing a way forward to avoid nonconservative analysis for low tension and pressure cases.

In Gaidai et al.'s work [15], the slip condition was calculated based on the mean static load conditions. However, for the case of significant dynamic tension, Grealish et al. [4] compared the fatigue life predicted from applying constant mean tension against that from applying dynamic tension and significant differences were found. It not only contributed to the alternating axial stress, but also influenced the friction slip conditions, which signified the importance of updating the slip conditions with respect to contact pressure variation.

In some tests, as reported by Skallerud [16], the moment-curvature relationship was observed to be frequency dependent. In Ozaki et al.'s work [17], an anisotropic friction model was formulated where the transition from static to dynamic friction was velocity dependent. However, this model was based on constant contact pressure while the contact pressure between layers is variable in the dynamic flexible pipe application. Therefore, this friction model has been modified in order to allow calculating the friction under variable contact pressure conditions.

As simplifications made in friction models should be minimized to ensure accurate prediction of fatigue life for arbitrary load conditions, the objectives of the present work are summarized as follows:

1. Present the most commonly used methods considering friction effect on the bending behavior of complex cross-sections.
2. Formulate friction models on the basis of constant shear interaction stick stiffness represented by the parameter, K_0, and dynamic contact pressure. The formulated friction models are implemented into a computer code.
3. Perform a sensitivity study to investigate the static friction effect with respect to the axial force of the element next to outermost fibre position.
4. Carry out a sensitivity study with respect to optimizing the parameter K_0 and validate a method to estimate this from bending moment test.
5. Propose a method based on the initial strain concept to reproduce the significant friction observed in the tests at small internal pressures and validate it against test measurements.
6. Carry out a friction model comparison study to investigate the static friction effect with regard to the bending moment-curvature relationship.

2. State of art

Fatigue analysis of flexible risers normally includes three steps: global analysis to obtain global curvature and tension time histories in representative sea states, local analysis transforming the global histories into stress histories at critical positions, and fatigue life evaluation by using the Palmgren Miner summation of damage from S-N curves. In local analyses, various methods are employed to treat the friction stress, which are summarized below.

2.1. Analytical method

In the model presented by Kavanagh et al. [1], the time dependent friction stress is taken as the minimum between the bending friction stress and sliding friction stress as expressed below:

$$\sigma_F(t) = min(\sigma_{FB}(t), \sigma_{FS}(t)) \tag{1}$$

The bending friction stress and sliding friction stress are expressed as follows:

$$\sigma_{FB}(t) = ER_L\kappa(t) \tag{2}$$

$$\sigma_{FS}(t) = \frac{\mu F_C(t)}{A} \tag{3}$$

where $F_C(t)$ is the time history of the contact force, $\kappa(t)$ is the time history of the global curvature, E is the Young's modulus of helix element, R_L is the helix layer radius, μ is the friction coefficient. The tension and global curvature time histories are obtained from time domain global analysis for each sea state.

2.2. finite element method

2.2.1. Stress transfer function

The method of stress transfer function which transforms the global curvature and tension time histories into stress time history of steel wires was stated, see Doynov et al. [18] and Wang et al. [19]. The local analysis can be carried out either by a 2D model for cases where the stress state is only determined by the global curvature and tension at selected positions, or by a 3D model if torsion coupling, longitudinal helix effects, long pitch lengths, local deformations (denting etc.) or boundary condition effects need to be considered.

In Doynov et al.'s work [18], two static runs were conducted, for minimum and maximum tension conditions, respectively. For each tension level, the friction stress-curvature relationship was obtained. Then the friction stress-curvature relationship corresponding to an arbitrary tension level was determined by linear interpolation between the relationship at the maximum tension level and the relationship at the minimum tension level. Good correlation was found between the application of the stress transfer function and the direct application of FE analysis.

2.2.2. Nonlinear bending moment-curvature model

For cases where 3D effects can be neglected, the 2D assumption can be applied to formulate a moment-curvature model. The moment-curvature relation can then be implemented into standard beam elements and the stress response calculated directly from global analysis, see Sævik [10].

2.2.3. Shear interaction model

For cases where 3D effects are significant, e.g., close to end fixations, the equilibrium equations must be based on handling each helix element individually, e.g., by sandwich beam theory. Then the slip behavior of each helix element is governed by a non-linear shear stress-relative displacement relationship. In the sandwich beam formulation the stress response will converge towards the plane surfaces remain plane solution in the stick domain if the parameter K_0 is infinite. Then the numerical value of K_0 must by selected as a compromise between accuracy and numerical stability [10]. One way of ensuring this is to apply an elastic-plastic shear stress and relative displacement relationship and tune the stick parameter Δ_1 in Figure 1 with respect to the mean static load condition, see Eq.4. However, for cases where dynamic tension is present (e.g., deep water applications), this will cause the parameter K_0 to vary, possibly introducing too low values at low contact pressures.
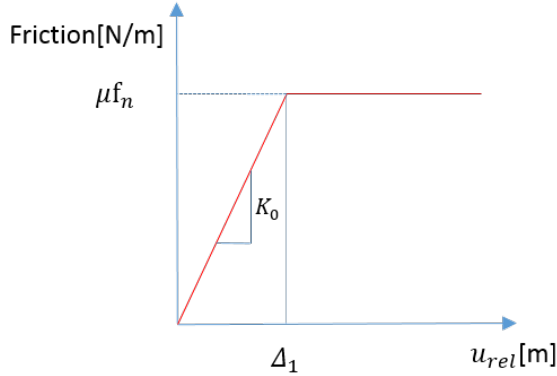
Figure 1: The related parameters of the shear interaction model

As seen in Figure 1, the relative displacement Δ_1 determines the onset of slip and remains constant in the numerical model. Then K_0 will be defined as:

$$K_0 = \frac{\mu f_n}{\Delta_1} \tag{4}$$

where $f_n = \oint \frac{p}{F_f}$. p is the nominal contact pressure and F_f is the fill factor of tensile armor.

The above methods cover the most commonly used ways to calculate friction in flexible riser structures. In conclusion, three factors determine the friction accuracy:

1. Alternating stick-sliding-restick conditions due to variable contact pressure conditions
2. Friction model
3. Criterion of sliding onset

3. Proposed friction models

Friction is mobilized along helices because of relative motion between two surfaces in contact. It acts in the tangential plane opposite to the direction of relative motion. Contact conditions can be divided into the stick and sliding (or slip) regimes depending on the relative motion magnitude. When the friction limit is reached, the static friction will transform into dynamic friction. As discussed in section 2, it is important to consider variable contact pressure condition because it determines the stick and sliding conditions, which is essential to precisely predict the friction in alternating conditions. It is hence essential to develop a realistic friction model, not only describing smooth transition from static to dynamic friction, but also considering the variable contact pressure condition. In addition, it is well known that helical elements in flexible risers basically slip along two routes: geodesic and loxodromic. The analytical analysis of local helix bending moments were initially developed by assuming that the helices follow the geodesic curve path in Feret and Bournazels' work [20]. However, transverse motion along the geodesic path can be eliminated even at small friction levels and Sævik [21] proposed that the loxodromic path was more realistic for dynamic load conditions. This has also been confirmed by numerical analysis, see Sævik [22]. For this reason, the friction along longitudinal direction, i.e., one dimensional friction, is focused on in this work. Some highlights of the formulated friction models are presented in Table 1.
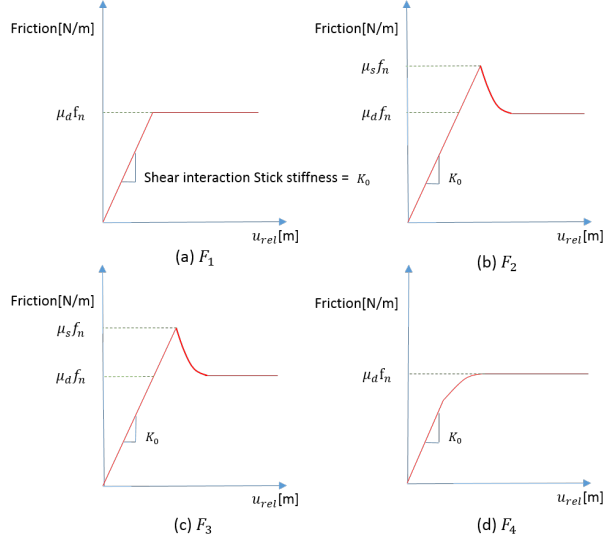
Figure 2: F_1-F_4 friction behavior introduction

Table 1: Brief descriptions of formulated friction models

Friction model name	Brief features of friction models
Coulomb friction model(F_1), see (a) in Figure 2	The static friction coefficient μ_s is equal to the dynamic friction coefficient μ_d, which means that the dynamic friction $\mu_d f_n$ is equal to the maximum static friction $\mu_s f_n$ and remains constant, where f_n is contact pressure.
Dynamic friction model(F_2), see (b) in Figure 2	This friction model describes a smooth transition from static to dynamic friction. It is based on realistic friction behavior described in literature[8]. Static friction drops significantly fast and approaches constant dynamic friction. The friction in the transition domain is only dependent on sliding velocity.
Static friction model(F_3), see (c) in Figure 2	This friction model describes the same friction behavior as for the F_2 model except that the friction in the transition domain is dependent on the relative displacement instead of sliding velocity.
Smoothened Coulomb friction model(F_4), see (d) in Figure 2	This friction model describes a smooth transition from the maximum static friction to dynamic friction. The maximum static friction is smaller than dynamic friction. It is developed aiming to improve the convergence performance of the F_1 model.

Friction models, subsequently abbreviated $F_1 - F_4$ have been implemented in BFLEX[6] and all have the same features that the parameter K_0 is constant and friction is calculated under dynamic contact pressure conditions.

3.1. Coulomb friction model (F_1)

The Coulomb friction model is the most commonly used for the shear interaction formulation with analogy to the elastic-ideally plastic material model concept. When the maximum static friction is exceeded, the dynamic friction remains constant and same as the maximum static friction.

3.2. Dynamic friction model (F_2)

When there is relative motion between contact surfaces, stick and sliding are two distinguished situations. Before maximum static friction is exceeded by shear force, the relative movement will be restrained. After that, the helix elements start to slide on the contact surface. Constraints for the sliding condition were summarized in Litewka's work [23] based on the concept of plasticity. According to the approach with analogy to plasticity, the relative displacement u can be divided into an elastic part (superscript e) and a plastic part (superscript p), representing the stick and sliding conditions, respectively.

$$u = u^e + u^p \tag{5}$$

The elastic relative displacement is either zero or a small quantity from micro-displacement which corresponds to rigid-ideally plastic and elastic-ideally plastic material models, respectively. In the rigid-ideally plastic model, the constraint of relative tangential displacement is in the following form:

$$u_e = 0 \tag{6}$$

With analogy to the stress and strain relationship, the traction and relative displacement between two surfaces can also be modeled based on plasticity theory. In the penalty method, friction is defined as:

$$f = \alpha(u - u^p) \tag{7}$$

Where α is the penalty parameter [23]. In the penalty method, the constraint condition can only be satisfied when $\alpha = +\infty$. However, it is well known that the penalty parameter must be selected as a compromise by also considering convergence issues. Therefore, the constraint condition has to be fulfilled within a certain tolerance by selecting the penalty parameter value. This method constitutes an analogy to a more general elastic-ideally plastic material model, where the penalty parameter α is the counterparts of the elasticity modulus.

In a similar way, the velocity is additively decomposed into elastic and plastic parts :

$$v = v^e + v^p \tag{8}$$

The corotational rate of traction is given by:

$$\mathring{f} = \dot{f} - \Omega f \tag{9}$$

where the skew-symmetric tensor Ω is the spin describing the rigid-body rotation of the contact surface. In the present work, it is assumed to be zero because the co-rotated formulation is used in this work. The co-rotational rate of traction has the relation with velocity based on Eq.7 as follows:

$$\mathring{f} = \alpha v^e \tag{10}$$

3.2.1. Constitutive formulations

It is aimed to develop constitutive formulations to describe the sliding yield surface and plasticity flow rules for the dynamic friction model. These constitutive equations are formulated based on the unconventional plasticity theory extended by Hashiguchi, see [24, 25, 26].

The conventional Coulomb friction sliding surface with isotropic hardening/softening is defined in Eq. 11. The isotropic hardening/softening rule means that the yield surface remains the same shape but expands/reduces with increasing/decreasing friction.

$$f(||\boldsymbol{f_n}||, ||\boldsymbol{f_t}||) = F(H) \tag{11}$$

where $||\boldsymbol{f_n}||$ is the normal traction, $||\boldsymbol{f_t}||$ is tangential traction and the scalar H represents the isotropic hardening/softening variable and describes the expansion/contraction of the sliding surface with increasing sliding displacement.

The initial yield surface function determines the onset of the yield process. It is assumed that the friction coefficient does not change with increasing normal contact traction. As stated above, the friction coefficient decreases from the static value in the stick condition and approaches the dynamic value in the stationary sliding condition. The reduction was assumed to be caused by the contraction of the normal sliding yield surface, and the contraction meant the plastic softening due to sliding [25]. In the present dynamic friction model, the hardening function $F(H)$ is described by the variable friction coefficient. The yield condition for the sliding potential is assumed to be according to Ozaki et al.'s work [17]:

$$f = \mu \tag{12}$$

It means that f designates the shape of sliding potential and μ describes the size of the normal sliding yield surface. Its initial value should be the static friction coefficient because the initial yield surface starts at the point when static friction is exceeded by the shear force.

The evolution of normal sliding yield surface was considered to predict the dynamic friction behavior in Eq.13 [25]. It is described by the evolution of the friction coefficient which is assumed to be according to [17]:

$$\frac{1}{f_n}\dot{f}_t = \dot{\mu} \tag{13}$$

$$\dot{\mu} = -\kappa\left(\frac{\mu}{\mu_d} - 1\right)^m ||\boldsymbol{v}^p|| \tag{14}$$

where μ_d is the dynamic friction coefficient, μ is the friction coefficient in the transition domain. κ and m are the parameters which affect the rate of hardening function because of the plastic sliding and rate of relative displacement [26].

The material time derivative of friction takes the form of Eq.10, if the rigid body rotation of contact surface is neglected. The plastic sliding velocity is assumed according to the sliding flow rule [17]:

$$\boldsymbol{v^p} = \lambda\boldsymbol{p} \tag{15}$$

where $\boldsymbol{p}$ is the sliding unit vector and λ is positive. In general, the sliding unit vector $\boldsymbol{p}$ is not in line with the tangential vector $\boldsymbol{f}$. In the present study, since only longitudinal friction is considered, $\boldsymbol{p}$ is in the longitudinal direction coinciding with direction of friction. The proportionality factor λ is obtained by Eq.13, Eq.14 and Eq.15. It is expressed in terms of sliding velocity as follows:

$$\lambda = \frac{\frac{\alpha}{f_n}}{\frac{\alpha}{f_n} - \kappa\left(\frac{\mu}{\mu_k} - 1\right)}v \tag{16}$$

$$
\begin{aligned}
\dot{f}_t &= \alpha(v - v_p) = \alpha(v - \lambda) \\
&= \left(\alpha - \frac{\frac{\alpha^2}{f_n}}{\frac{\alpha}{f_n} - \kappa\left(\frac{\mu}{\mu_k} - 1\right)}\right)v \\
&= Kv
\end{aligned}
\tag{17}
$$

8

$$\dot{f}_t \Delta t = K v \Delta t$$
$$\Delta f_t = K \Delta u \tag{18}$$

where K represents the stiffness in the transition domain, κ is the linear slope from the static to the dynamic friction coefficient within the transition distance. Its value should be obtained by friction tests.

3.2.2. Discussion

There are two ways to calculate the friction:

1. Accumulate the friction at load step i by using the friction and the stiffness K in load step $i - 1$, i.e., $f_t^i = f_t^{i-1} + K^{i-1}\Delta u$
2. Calculate the friction coefficient μ^i based on the relative displacement at load step i and update the friction using $f_t^i = f_n^i \mu^i$

As to the first method, the smooth transition from the static to dynamic friction can be achieved by the transition stiffness matrix. However, the friction along the normal-sliding surface can only be obtained from the updated stiffness matrix based on the friction in the last load step and would lead to load step resolution dependency and be limited to constant contact pressure conditions when implemented into a finite element model. Therefore, only the second method is considered in the following.

Figure 3 shows the effect of dynamic contact pressure and velocity on the friction behavior. In all simulations, μ_s and μ_d were set equal to 0.31 and 0.2, respectively. CT and VT denote constant and dynamic contact pressures, respectively, where the constant contact pressure was taken to be $2.0E4$, and the dynamic contact pressure was assumed to be a harmonic function $2.0E4 sin(t) + 2.0E4$ with unit $[N/m]$. For the constant contact pressure cases, two transition ratios were applied to simulate the friction in the transition domain where the transition ratio is defined as the ratio between the transition length and the elastic relative displacement. The transition ratio 2.0 was selected based on experience with friction testing where the ratio value generally depended on the local contact condition. For the constant contact pressure case, κ was assumed to be 8870 $[1/m]$ while κ was variable in the dynamic contact pressure case. The velocity amplitude v_1 was set to 2.2E-5 $[m/s]$. The velocity directly determines the transition distance which is the relative displacement distance from maximum static to constant dynamic friction. For the dynamic contact pressure case, the friction varies with varying contact pressure, which validates the second method to calculate the friction under dynamic contact pressure conditions.

3.3. Static friction model (F_3)

3.3.1. Constitutive formulations

The static friction model has the same behavior as the dynamic friction model except that the friction in the transition domain is only dependent on relative displacement. The friction yield line is therefore described by Eq.12. The yield line behavior, i.e., expanding or shrinking, can be described by variation of the friction coefficient μ. The derivative of the yield line with respect to the relative displacement is formulated as:

$$\frac{1}{f_n}\frac{df_t}{du} = \frac{d\mu}{du} \tag{19}$$

whereas the derivative of the friction coefficient μ with respect to the relative displacement reads:

$$\frac{d\mu}{du} = 2\kappa \frac{u_p - u}{u_p - u_e} \tag{20}$$

$$\kappa = \frac{\mu_s - \mu_d}{u_e - u_p} \tag{21}$$

9
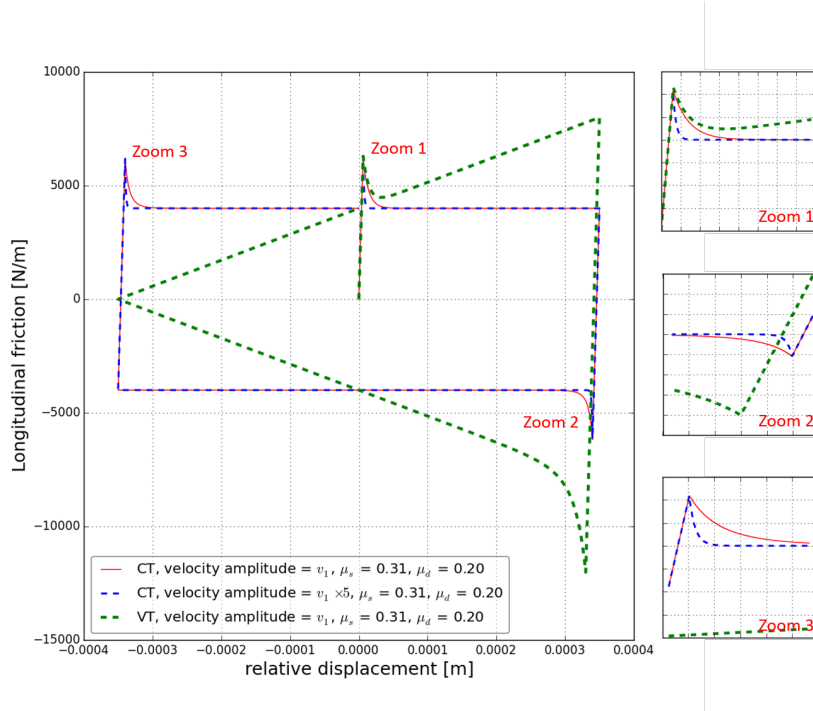
Figure 3: Dynamic friction model

where κ is the linear slope from the static to the dynamic friction coefficient. Then the transition stiffness K in the transition domain can be obtained by the application of Eq.19 and Eq.20 as:

$$
\begin{aligned}
\frac{df_t}{du} &= 2\kappa \frac{u_p - u}{u_p - u_e} f_n \\
df_t &= K\,du
\end{aligned}
\tag{22}
$$

3.3.2. Discussion

The friction coefficient was assumed to be independent on contact force and obtained by integrating Eq.20 from the elastic relative displacement to the relative displacement at load step i. Therefore, the friction at load step i was independent on the friction history. At the same time, the transition stiffness K can be updated by Eq.22. In Figure 4, the effect of the transition distance, load step resolution and dynamic contact pressure on the friction behavior is presented, applying similar input data as for the F_2 model. For the constant contact pressure cases, two transition ratios were applied to simulate the friction in the transition domain. κ is then directly determined by the transition distance, see Eq.21. In addition, a simulation by applying 10 times less load step resolution was included. It is seen that the friction with full resolution and 10 times less resolution of relative displacement coincides with each other, demonstrating that the static friction model is load step resolution independent. For the dynamic contact pressure case, the friction varies with variable contact pressure, which proves that this friction mode is able to consider the friction under variable contact pressure, as shown by the thick dotted line in Figure 4.

3.4. Smoothened Coulomb friction model (F_4)

3.4.1. Constitutive formulation

The smoothened Coulomb friction model F_4 is developed to benefit the convergence performance of the F_1 model. The description of yield line and derivative of yield line are the same as for the F_3 model as

10
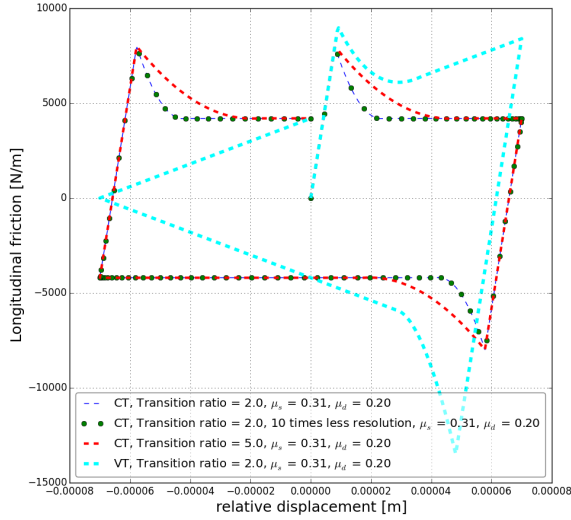
Figure 4: Static friction model

formulated in Eq.12 and Eq.19. The derivative of friction coefficient in terms of relative displacement μ also takes the form of Eq.20.

3.4.2. Discussion

In this section, the effect of load step resolution and dynamic contact pressure on the friction behavior is investigated using similar input data as for the F_2 model. As seen in Figure 5, the friction applying full resolution and 10 times less resolution of relative displacement gives the same results, stating that the F_4 model is load step independent. The friction can also be correctly predicted under dynamic contact pressure, shown by the dotted line in Figure 5. The dynamic contact pressure was set to be same as applied for the F_2 and F_3 models.

4. Results and discussions

The friction models $F_1 - F_4$ were implemented into the HCONT453 and HCONT463 contact elements in BFLEX [6] and applied for numerical studies. HCONT453 is a four node contact element for handling contact between two helix layers, whereas HCONT463 considers contact between a cylindrical layer and one helix layer. They are both based on a hybrid mixed formulation where the contact condition is imposed by means of a penalty surface stiffness parameter [6].

The models presented herein also makes use of the structural elements HSHEAR353 and HSHEAR363. HSHEAR363 is a 13 degrees of freedoms (DOFs) element that in addition to the 12 standard beam DOFs includes a radial DOF to describe radial interaction. Two constitutive models are allowed for: one thin shell model for representing the plastic layers and one helix model to represent the axisymmetric forces in the pressure spiral layers. HSHEAR353 is a 24 DOFs curved beam element that in addition to the standard beam DOFs includes 12 local helix DOFs to describe the local displacement relative to the loxodromic path, see [6, 27, 28]. These elements can be applied for modeling all layers in a flexible pipe.
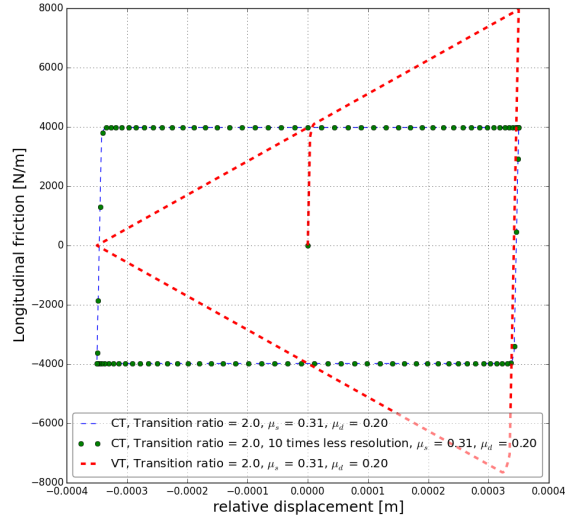
Figure 5: Smoothened friction model

4.1. Investigation of shear interaction stick stiffness influence

The purpose of this example is to investigate the shear interaction stick stiffness parameter, K_0, effect with respect to accuracy by investigating the element axial force next to the outermost fibre on the tensile side of the pipe.

4.1.1. Description of numerical model

A simple numerical model was established. The model consisted of a single tendon with 35° lay angle and 73 mm layer radius, and one helix supporting layer which had the same geometry and arrangement as for the tendon. The tendon's cross-section was 5 mm wide and 2 mm thick. The length of the model represented a half pitch of tendon applying 20 elements. The HSHEAR353 curved beam element was used to model the tendon and the supporting structure. The HCONT453 contact element was further used to model the contact between the tendon and the supporting layer based on the sandwich beam approach, see Sævik and Ye [29].

Both ends of the supporting layer were fixed and other elements were designated to slide according to prescribed harmonic displacement to simulate the relative displacement induced by cyclic bending loads. A concentrated axial force of 1000 N was applied at the right end of tendon to provide contact pressure. Then the right end was fixed in order to realize the relative displacement between two layers. Both the tendon and the supporting layer were fixed in the transverse direction since only longitudinal friction was considered.

4.1.2. Discussion

The internal friction before slip results in a high stick bending stiffness in the global moment-curvature relation. The parameter K_0 is obtained based on the assumption of plane surfaces remain plane, which is elaborated in detail in Sævik's work [10]. In his work, K_0 was analytically expressed as:

$$K_0 = \gamma \frac{EA \sin^2 \alpha}{R^2} \tag{23}$$

In which γ is a scaling coefficient applied to obtain the plane surfaces remain plane assumption before slip occurs. E is the steel wire's Young's modulus, A is the steel wire's cross-section area, α is steel wire's lay

12

angle and R is the tensile armor layer mean radius. The parameter K_0 is a key parameter determining the stick bending stiffness. In order to quantify K_0 or determine how to select γ, a sensitivity study was carried out. In this study, it was aimed to compare the axial force of the element next to the outermost fibre by using different K_0 values.

Nine shear interaction stick stiffnesses were used in the sensitivity study. A K_0 value of 5E4 $[MN/m^2]$ that is 238 times the value with γ equal to 1.0 was regarded as an infinite value and the axial force obtained from the simulation with this infinite value was selected as a reference value. The axial force attained based on all other K_0 values were then compared against the reference value. The deviation σ in terms of axial force was calculated using the values obtained along the straight vertical line in Figure 6 and expressed as:

$$\sigma = \frac{N_{reference} - N_i}{N_{reference}} \tag{24}$$

where i ranging from 1-8 denotes alternative K_0 values and $N_{reference}$ refers to the reference value of axial force obtained in the simulation with infinite K_0. The comparison of axial forces based on different K_0 values is depicted in Figure 6 whereas the deviations are summarized in Table 2. It is concluded that the accuracy obtained by applying $\gamma = 12$ to ensure numerical stability as proposed by Sævik and Ye [29] is satisfactory, giving a maximum deviation of 8%.
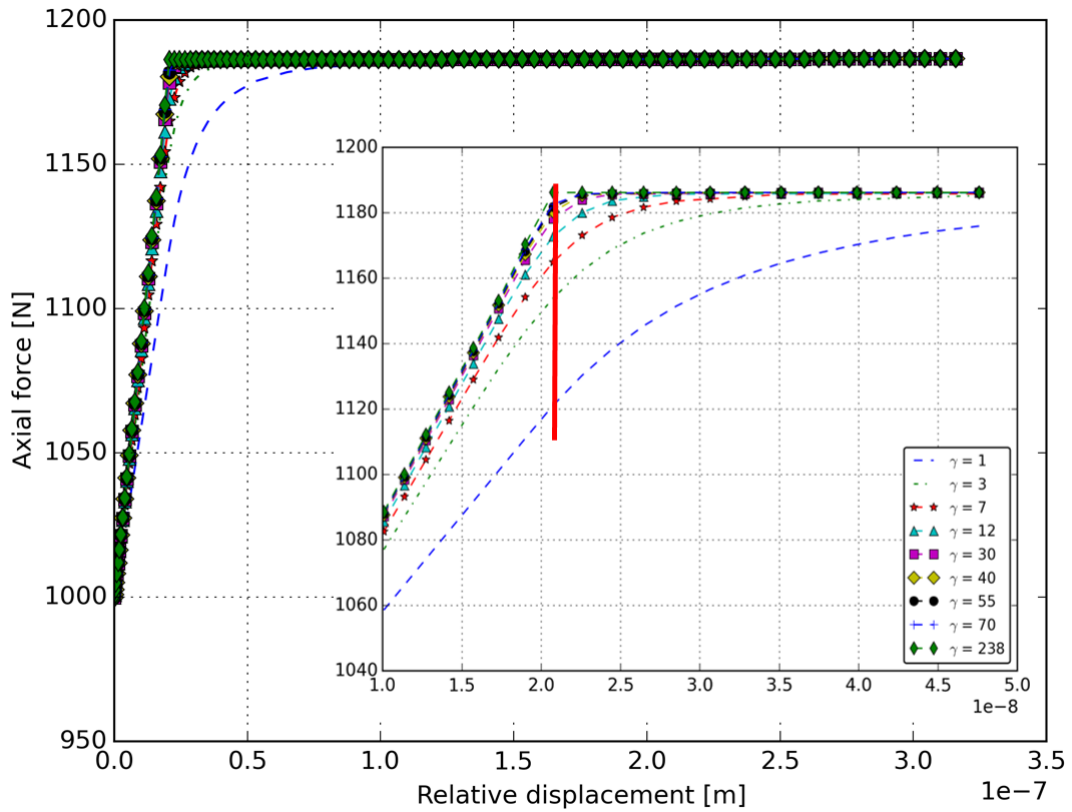

Figure 6: The effect of shear interaction stick stiffness on the tendon's axial force next to the outermost fibre position

Table 2: Shear interaction stick stiffness sensitivity study

γ	70	55	40	30	12	7	3	1
Deviation, σ	3%	3%	4%	5%	8%	12%	18%	35%

4.2. Effect of proposed friction models on tendon's axial force

4.2.1. Comparison between friction models

In this section, the effect of the static friction coefficient on tendon's axial force is focused on. The same numerical model as described in section 4.1.1 was applied. The dynamic friction coefficient was set to 0.2 and the transition distance from the static to dynamic friction in the F_3 and F_4 models were assumed two times the maximum elastic stick displacement in all cases.

The friction force next to the outermost fibre position obtained by the proposed friction models and by application of different static friction coefficients, μ_s, is shown in Figure 7. The contact line force (force per unit length) is variable during a full cyclic motion. The static contact line force due to the constant concentrated load 1000 N was about 5050 $[N/m]$ while the dynamic contact force was approximately 800 $[N/m]$. The friction history confirms the validity of friction models under variable contact pressure conditions.

Figure 8 shows the time histories of friction and the corresponding contact line load for nine contact elements along the helix path from the outermost fibre to the neutral axis position. Also the axial force histories in the corresponding helix beam elements are included in the same figure. The friction model was activated at 5.01s in the numerical model. The friction at different positions are variable due to different levels of contact line force. The shear force capacity governed by friction is exceeded starting from the element at the neutral axis represented by the "Element 10" in the legend of Figure 8 while the other elements are still in the stick domain. The full slip condition was achieved at 5.26s when all elements reach the dynamic friction regime. It is observed that when the friction force next to the outermost fibre position enters the slip domain represented by "Element 2", the friction forces along the path approaching the neutral axis have already entered into the slip domain, acting to reduce the influence from static friction with respect to the tendon axial force. By considering the bending moment of a full flexible pipe cross-section, the situation will be similar as each tendon will be in different slip regimes, thus acting to reduce the influence of static friction, which will be discussed in section 4.3.

The effect of applying the proposed friction models with respect to the tendon's axial force is demonstrated in Figures 9 and 10. As illustrated in Figure 9, the F_4 model gives almost identical axial force amplitude as compared to the F_1 model. In both cases, the axial force amplitude is determined by the dynamic friction for large slip amplitudes. The only difference is that the axial force obtained from the F_4 model in the transition domain is smaller than for the F_1 model, where the static friction coefficient in the F_4 model is set to 10% smaller than for the F_1 model (0.18 versus 0.20). It has no effect on the maximum axial force amplitude, and the transition domain where the axial force is underestimated is quite small. Considering that in practical fatigue calculations, the stress ranges will be distributed in the entire stick-slip domain, it is concluded that the F_4 model can produce results with sufficient accuracy as compared to the F_1 model as long as the static friction coefficient is not taken to be less than 90% of the dynamic friction coefficient. From the simulated response in terms of the axial force amplitude by applying alternative static friction coefficients, i.e., 0.21, 0.22, 0.23, it reveals that the axial force amplitude is primarily influenced by the dynamic friction, as a 15% increase in static friction only causes the axial force amplitude to be approximately 3% larger.

Figure 10 presents the influence of applying the static and dynamic friction models on the axial force at the outermost fibre position. The static friction coefficient was set to 0.23 and 0.31, respectively. The dynamic friction coefficient was assumed to be 0.2 in all cases. The transition distance in dynamic friction model is observed to be larger than for the static friction model as shown in Figure 7. That is the reason why

14
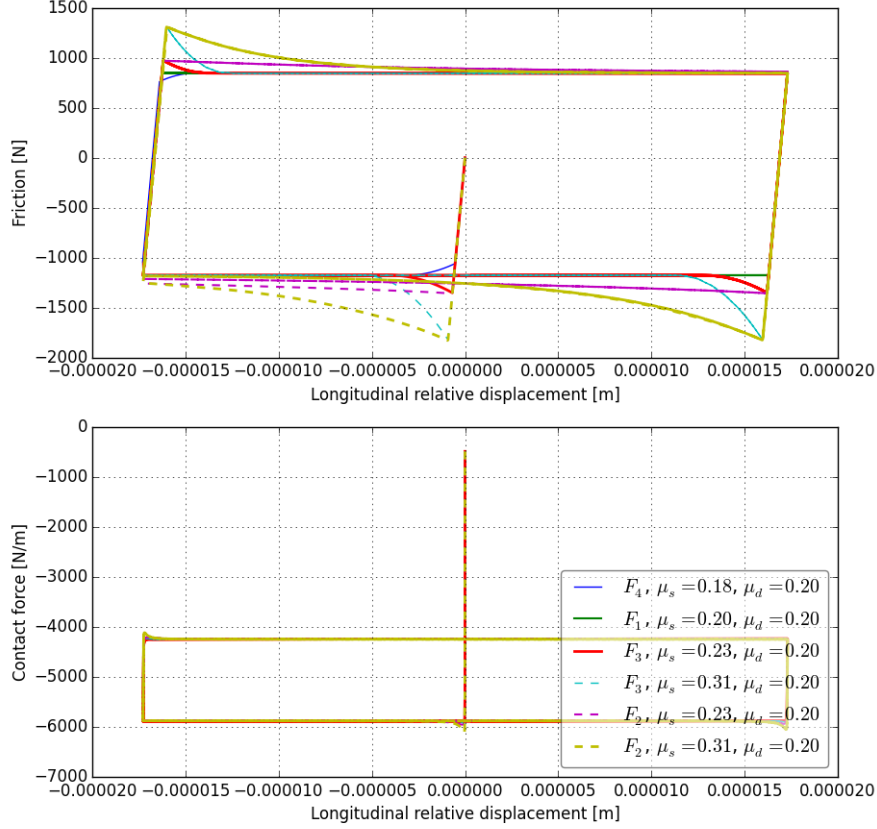
Figure 7: Friction behaviors of the contact element next to the outermost fibre position by applying friction models F_1-F_4

longer transition in the axial force history is observed for the dynamic friction model in Figure 10. In both cases, the axial force amplitudes are primarily determined by the dynamic friction as a 50% increase from the dynamic to static friction coefficient (from 0.2 to 0.31) only gives a 6% increase in the force amplitude at the tensile side. On the compressive side, the difference is even smaller due to the decease in contact pressure, thus acting to further reduce the influence of static friction. This demonstrates that the effect of static friction on the axial force is relative small due to the process of subsequent slip and transition into the dynamic friction domain along the helix path. This also suggests that the standard industry practice of combining a Coulomb friction model with a friction coefficient set to the average between static and dynamic friction will be on the conservative side.

4.3. Validation of proposed friction models against experimental data

Full scale tests were carried out by MARINTEK in 1991-1992 [14] to investigate damping properties of dynamic flexible pipes. In the present study, the test data were applied to verify the proposed friction models by comparing the global response obtained from the numerical analysis against the test results. In the test, parameter variation with respect to loading frequency, internal pressure and global curvature range were conducted.
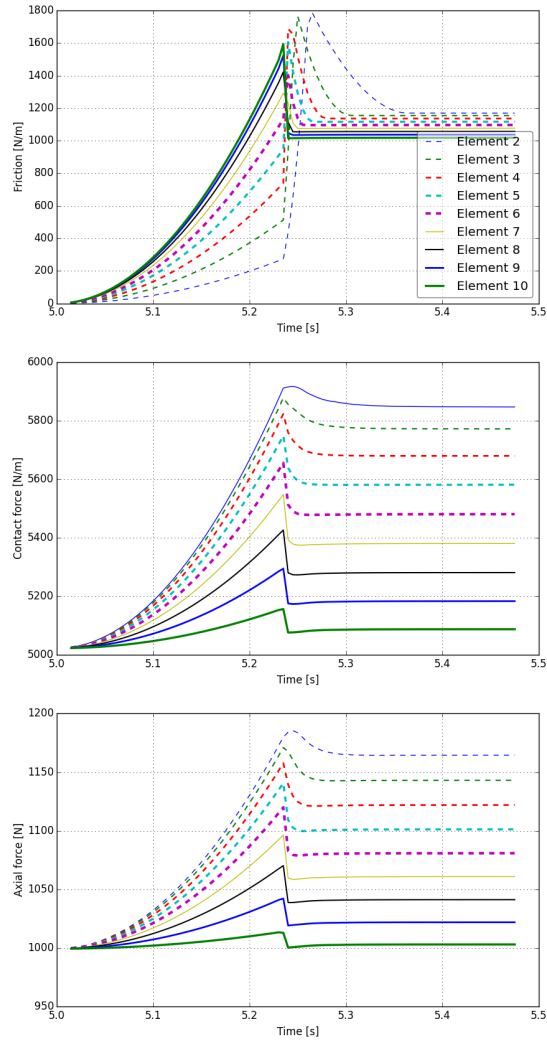
Figure 8: Time histories of friction and the corresponding contact line load for nine contact elements along the helix path from the position next to the outermost fibre to the neutral axis position and time histories of tendon's axial force for the beam element.

4.3.1. Description of numerical model

A sketch of the test set-up is shown in Figure 11. The whole length of the 4 inch flexible pipe was 8 meters and it was horizontally mounted in a test rig. It was equipped with end fittings at both ends. In the bending tests, two halves of tubes were clamped on the pipe at 1.35 meter from the right end. This allowed the pipe to be treated as a cantilever beam. Two extensometers were attached at the two outermost fibre positions of the pipe to measure the curvature at 1.19 meter from the right end. The curvature was calculated based on the measured axial strain and outer diameter of the pipe by using $\frac{\epsilon_{top} - \epsilon_{bottom}}{D}$. The test was run in displacement control where the displacement was applied at the right end. The reaction force was recorded by an actuator. Therefore, the global bending moment of the pipe was simply obtained by the reaction force from actuator and the 1.19m length at the measurement location.

A model of the test specimen was established in BFLEX. The model included the activated length of 1.35m only. The tensile armor's lay angle was $\pm 38°$ and the pitch length was approximately 0.57m. The friction models parameter K_0 was assumed to be 1730 $[MN/m^2]$ according to the sensitivity study in section 4.1. The pipe cross-section consisted of two cross wound tensile armor layers, four plastic sheath layers including the outer sheath and two anti-wear layers and one pressure barrier. For both the inner and outer tensile armor layer, HSHEAR353 was employed to model the individual steel wire and 16 steel wires were used to represent the whole tensile armor layer. HCONT453 was applied to simulate the contact surface between these two tensile armor layers. HSHEAR363 was used for the plastic layers and pressure spiral layer. HCONT463 was applied to simulate the contact surface between the cylindrical layer and the tensile armor layer. Both ends of the steel wires in the tensile armor layers were fixed in relative displacement (between the supporting layers and the wire). Then the centerline beam degrees of freedom were fixed in the left end and free in the other end except for the vertical direction where a prescribed vertical displacement was imposed. Other inputs are summarized in Table 3 and the FE model is shown in Figures 12 and 13.

Table 3: Key input parameters of full scale numerical model

Parameter	Value	Unit
Barrier (Core) mean radius	58.3	mm
Pressure spiral mean radius	64.05	mm
Anti-wear tape 1 mean radius	68.2	mm
Anti-wear tape 2 mean radius	72.2	mm
Inner tensile armor mean radius	70.3	mm
Outer tensile armor mean radius	74.3	mm
Tape (Nylon)	75.4	mm
Plastic layers' Young's modulus	1100	MPa
Outer sheath mean radius	78.55	mm
Pressure spiral area	35	mm^2
Steel wire's Young's modulus	210	GPa
Inner/outer tensile armor area	10	mm^2
Inner/outer tensile armor lay angel	-38/38	deg
Number of inner tensile armor	61	
Number of outer tensile armor	65	

The key factor which affects the global response of the flexible pipe is the friction property of the contact surfaces between layers. The pipe had two layers of anti-wear tapes at both inner surfaces of the tensile armor layers. The friction coefficient between anti-wear tape and inner armor, and between two layers of steel armors was estimated to be 0.20 at 20 MPa internal pressure, see Sævik [21]. This friction coefficient has, however, been varied to obtain a best fit with regard to the test data for different internal pressure, see section 4.3.5.

Five tests were carried out to study the hysteresis behavior due to the internal slip mechanism. The test program is listed in Table 4. Tests No.1-2 were intended to study the influence of loading frequency on the hysteresis behavior at low and high internal pressures, respectively. Tests No.3-5 were conducted to study the effect of internal pressure on the hysteresis behavior with constant frequency 0.1 Hz. For all cases the motion was controlled by a sinusoidal input signal.

Table 4: Test matrix

Test No.	Target curvature [1/m]	Internal pressure [MPa]	Frequency [Hz]	Prescribed displacement [mm]
No. 1	1/17	0.7	0.1	40
No. 2	1/17	0.7	0.5	40
No. 3	1/9	0.7	0.1	70
No. 4	1/9	10	0.1	70
No. 5	1/9	20	0.1	70

The Coulomb friction F_1 model was applied for investigating end effects, validating the method of estimating the parameter K_0, investigating initial strain of outer sheath and studying the effect of friction coefficient as respectively reported in sections 4.3.2, 4.3.3, 4.3.4 and 4.3.5. Static friction F_3 and smoothened Coulomb friction F_4 models were additionally applied to investigate the friction coefficient effect on the bending moment-curvature relation, see section 4.3.6. With respect to the F_3 model, the ratio of transition distance and elastic relative displacement was assumed to be 2.0.

4.3.2. Sensitivity study of end effect

The clamped tubes restrained the rotation of the pipe and axial displacement of the outer sheath. However, the tendons can move freely inside. Therefore, springs were applied in the numerical model to fulfill the boundary conditions in the test setup considering the full length of the flexible pipe. Spring nodes were therefore generated at the same coordinates as for the left end tendons. Spring elements were then connected between the spring nodes and the tendons nodes to reflect the total model length. The spring element axial stiffness was calculated as follows:

$$K_s = \frac{EA}{L}f \tag{25}$$

where EA is axial stiffness of the tendon, L is the length of the tendon, i.e., $L = \frac{8-1.35}{cos\alpha}$, α is the lay angle and f is the ratio between the number of tensile armors in a layer and the number of tensile armors used to represent that layer. In this case, 16 tensile armors were simulated and the scale factor was about 4.0. A sensitivity study of spring axial stiffness was carried out as seen in Figure 14. A relative large spring stiffness 12000 $[MN/m]$ for simulating fixed boundary conditions and a relative small value 120 $[MN/m]$ simulating axial free conditions were used whereas the 976 $[MN/m]$ value was obtained from Eq.25. The spring axial stiffness significantly influences the curvature distribution along the model length. The curvature inflection is caused by the steel wires acting as 3D structures exposed to a given set of boundary conditions. This causes a harmonic curvature variation and a concentration of curvature at the left end fixation. The measured position was located 0.16 m away from the left end. As illustrated in Figure 15, the spring axial stiffness also affects the friction moment and the bending stiffness in slip domain at the measurement location.

4.3.3. Determination of the shear interaction stick stiffness

When the tensile armor is supported by thick plastic layers, shear deformations will occur in the plastic layers and the assumption of plane surfaces remain plane is not valid before slip starts. Then the task is to quantify the parameter K_0 which combines the contributions both from internal friction and the shear deformation of plastic layers, which yields:

$$\frac{1}{K_0} = \frac{1}{K_{friction}} + \frac{1}{K_{shear}} \tag{26}$$

where K_0 is the shear interaction stick stiffness applied in friction models and can be verified by the stick bending stiffness in the bending moment-curvature relationship, $K_{friction}$ is the shear interaction stick stiffness governed by the internal friction properties and K_{shear} is the shear stiffness due to the deformation of the plastic layers. The part related to internal friction $K_{friction}$ was determined by the sensitivity study in section 4.1.2. The shear stiffness K_{shear} was formulated by Sævik and Li's work [22] where the shear stiffness was proposed as:

$$K_{shear} = \frac{Gb}{t} = \frac{E_p b}{2(1+\nu)t} \tag{27}$$

where E_p is Young's modulus of the plastic tape, G is the shear modulus of the plastic layer, b is the width of the tendon, ν is the Poisson's ratio, t is the thickness of the plastic layers. The plastic layer thickness was assumed to be 5.1 mm+2.0 mm corresponding to the thickness of the inner sheath and anti-wear tape beneath the inner tensile armor, respectively. This gives a shear stiffness of 221 $[MN/m^2]$. A validation study was conducted by means of numerical simulations for Test No.5, see Table 5.

Table 5: Shear interaction stick stiffness matrix

Shear interaction stick stiffness $[MN/m^2]$	Brief description
17300	K_0 for Eq.23 with $\gamma = 120.0$
1730	K_0 for Eq.23 with $\gamma = 12.0$
221	shear stiffness for plastic layers
196	K_0 by combining 1730 $[MN/m^2]$ with 221 $[MN/m^2]$

The simulation results with respect to parameter K_0 are presented in Figure 16. It is clearly seen that good agreement in terms of stick bending stiffness is obtained by applying the K_0 value of 196 $[MN/m^2]$.

4.3.4. Investigation of outer sheath's initial strain

The outer sheath provides a seal against sea water aiming to prevent the inner structures of flexible pipes from corrosion. In addition, it contributes to the bending stiffness of the pipe. The outer sheath is extruded on the surface of the outer layer of tensile armor resulting in an initial tensile stress as a result of the cool-down process and the constraint from other layers. As seen in Figure 17, there is significant hysteresis at 0.7 MPa pressure for Test No.3. Prior to the model calibration study at different pressure levels, a static FE analysis was carried out at 0.7 MPa internal pressure to determine the amount of initial strain in the outer sheath needed to reproduce the moment-curvature behavior of Test No.3, see Table 4. The Coulomb friction model was applied in this study using the friction coefficient 0.26.

Good agreement between simulation results and test measurements was obtained assuming an initial strain of 0.02 in the outer sheath, see Figure 17. This demonstrates that the initial strain concept can be applied to explain the significant friction observed at small internal pressure. The corresponding initial stress was found to be 9.7 MPa which was considered to be reasonable. Figure 18 shows the influence of different initial strain values on the friction moment behavior at 20 MPa. It is seen that by increasing initial strain,

the friction moment will increase, whereas the bending stiffness in the slip domain remains the same.

4.3.5. Investigation of friction coefficient

The amount of initial strain 0.02 was determined by obtaining good agreement between the test measurements and the numerical model at internal pressure 0.7 MPa (Test No.3 shown in Figure 17). The Coulomb friction model F_1 was applied where the friction coefficient was set to 0.26. As seen in Figure 19, this also gave good correlation for Test No.1 corresponding to the smallest applied curvature range for the 0.7 MPa cases in Table 4. However, the friction coefficient had to be tuned to 0.23 and 0.21 to get a best fit with respect to the elevated pressure cases Test No.4 at 10 MPa and Test No.5 at 20 MPa, see Figures 20 and 21. As reported in Dunkin and Kim's work [30], the friction coefficient decreased with increasing contact pressure. In addition, the contact surface is characterized by the texture of steel wire and the plastic tapes. Different contact pressure levels induced by the internal pressure determine the degree of full contact conditions between layers and it hence determines the different texture of the contact surfaces. Further more, there are inherent misalignments between the steel wires and plastic tapes due to the manufacturing procedure, which would also alter the contact surfaces conditions. Therefore, the friction coefficient may vary at different contact pressure levels as observed in Tests No.3-5.

The effect of the friction coefficient on the moment-curvature behavior is shown in Figure 22, demonstrating that if the selection of friction coefficient is based on friction tests at too low contact pressure, this would have the potential of overestimating the real friction moment during high pressure conditions.

4.3.6. Investigation of proposed friction models

The static friction F_3 and smoothened Coulomb friction F_4 models were employed in this study. Experience obtained by friction testing has revealed that the static friction coefficient may be up to 50% above the dynamic value. The static and dynamic friction coefficients were therefore assumed to be 0.31 and 0.21, respectively for the F_3 model whereas for the F_4 model, the corresponding values were set to 0.18 and 0.21, respectively. For F_3 model, the static friction coefficient value of 0.24 was additionally included. As shown in Figure 23, the bending moment in the slip domain is mostly governed by dynamic friction since the bending moment histories in slip domain in all cases coincide with each other. Comparing the friction moment behavior applying the F_4 model with $\mu_s = 0.18$, and the F_3 model with $\mu_s = 0.31$, it is seen that the moment is only 6% higher when applying $\mu_s = 0.31$. This confirms the behavior observed for the simplified model in section 4.2.1 and being explained by the subsequent slip along the helix path is also confirmed by the test results.

5. Conclusions and future work

In this work, the most commonly used methods to deal with the friction effect in non-bonded flexible pipes were summarized. Four friction models were formulated and then implemented into a computer code. The friction models included both static and dynamic friction effects. In addition, they were designed to have constant shear interaction stick stiffness and smooth transition from static to dynamic friction as well as enabling continuously update under dynamic contact pressure conditions.

A sensitivity study of the shear interaction stick stiffness parameter, K_0, was conducted. It was demonstrated that the K_0 proposed by Sævik and Ye [29] for the assumption of plane surfaces remain plane was satisfactory with respect to the accuracy. A comparison study was then carried out to investigate the effect of different friction models on the tendon's axial force next to the outermost fibre position at the tensile side. It was found that the smoothened Coulomb friction provided almost identical axial force amplitude when compared to the Coulomb friction model, however, the former being beneficial with respect to convergence

issues. The amplitude of axial force was found to be mostly governed by dynamic friction as the axial force next to the outermost fibre position with a static friction coefficient of 0.31 was found to be only 6% larger than when applying the static friction coefficient of 0.21. This was found to be due to the subsequent slip process along the helix path, thus reducing the influence of the static friction coefficient.

In the full scale tests, pronounced hysteresis in the moment-curvature relation under small internal pressures was observed. Therefore, the initial strain concept was proposed and applied in the numerical model to obtain a correct amount of pre-stress in the outer sheath. Good agreement was found with respect to the friction moment as compared to the test measurements by applying this concept for reasonable values of prestress. The significant friction moment observed in the tests suggests that this effect should be included in fatigue calculations, which is not common practice today.

The friction coefficient needed to obtain good correlation as a function of internal pressure was determined by comparison against test data. The friction coefficient had to be slightly tuned to obtain a best fit under different internal pressure conditions. The friction coefficient for the tests investigated was found to be in the range 0.21-0.26 depending on the internal pressure level signifying the importance of applying realistic contact pressure during friction testing. The smoothened Coulomb friction and static friction models were employed for the comparison study. It was concluded that the moment in the slip domain was mostly governed by dynamic friction in accordance with both the findings obtained from the simplified model and the full scale test results. In addition, as only 6% increase in the tendon's axial force amplitude applying 50% increase in the static friction coefficient sensitivity study, it concluded that the standard industry practice of combining a Coulomb friction model with a friction coefficient set to the average between static and dynamic friction will be on the conservative side.

For future work, it is of interest to measure the static and dynamic friction coefficients, the transition distance between them and frequency effects by small scale testing. In addition, means of validating the shear stiffness by small scale testing should be investigated. If this can be found from small scale testing, it would be a cost effective way of estimating the shear interaction stick stiffness without performing full scale tests. The behavior during bi-directional slip and the influence of inherent anisotropy should be also investigated as only longitudinal slip was included in the present study.
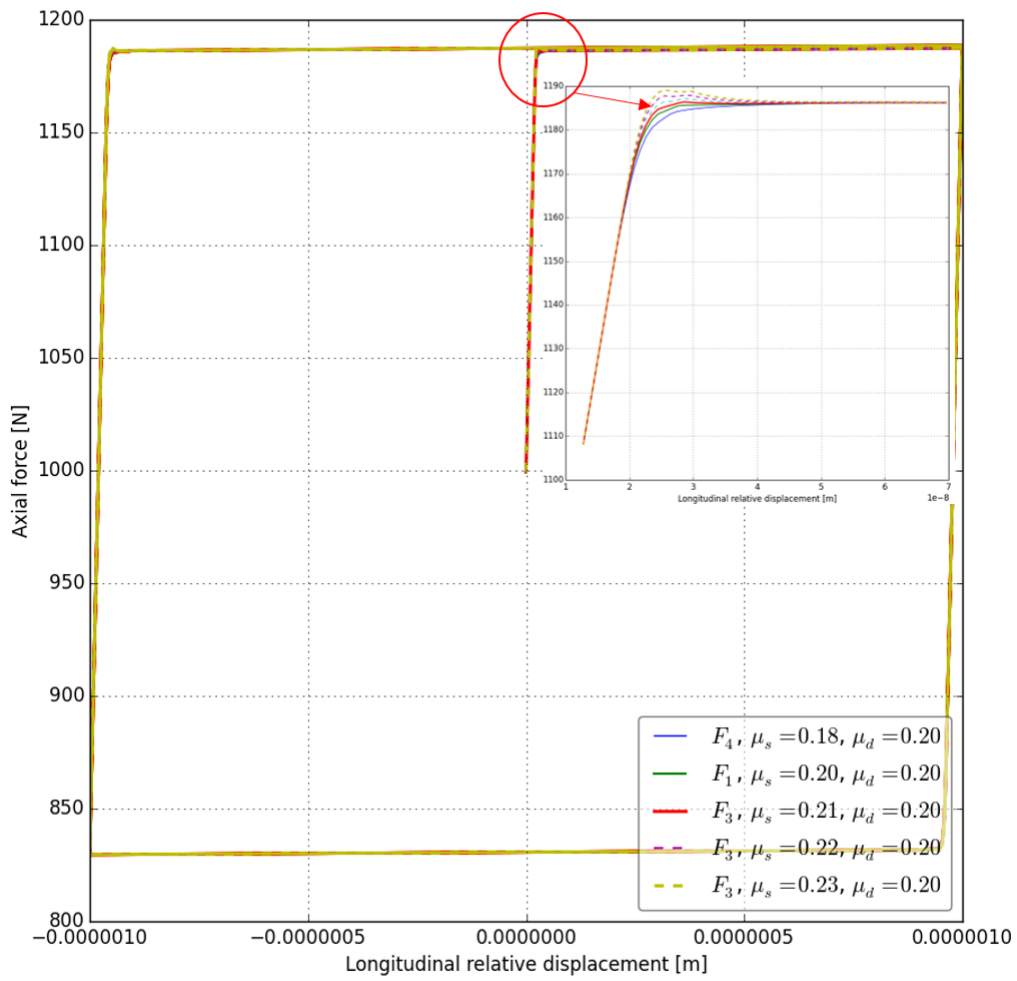
Figure 9: The effect of friction models (Coulomb friction, static friction and smoothened Coulomb friction models) on the axial force of the tendon next to the outermost fibre position
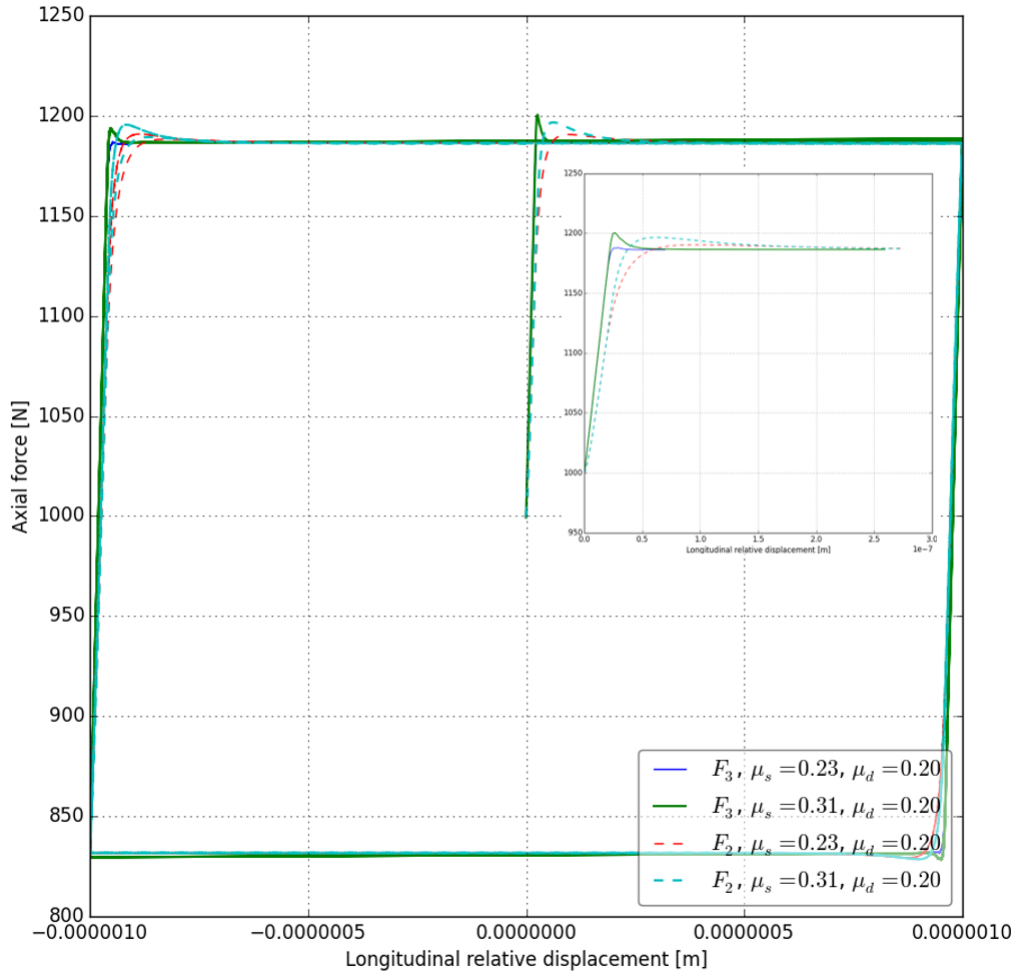
Figure 10: The effect of static and dynamic friction models on the axial force of the tendon next to the outermost fibre position
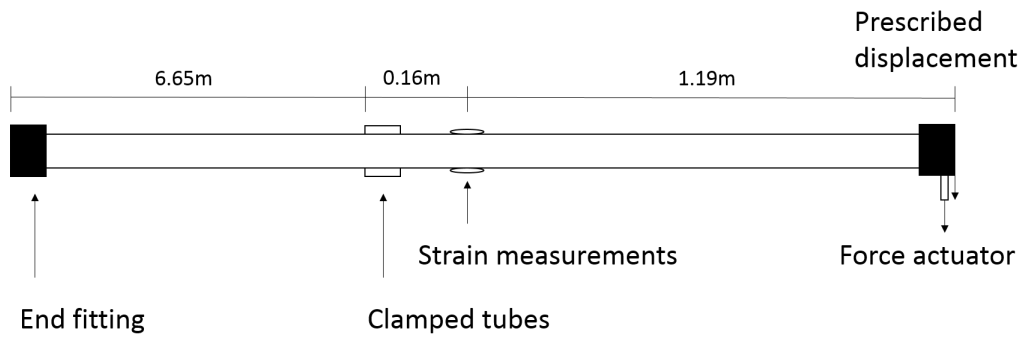

Figure 11: Full scale test setup

1. Flexible barrier

2. Pressure armor layer

3. Anti-wear tape

4. Inner tensile armor

5. Anti-wear tape

6. Outer tensile armor

7. Nylon tape

8.Outer sheath Polyethyiene
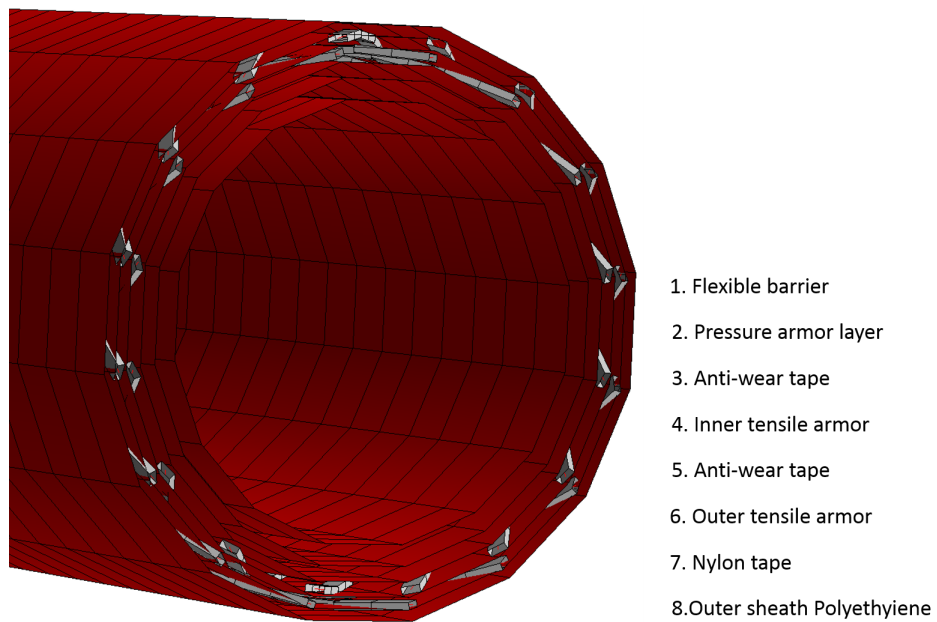
Figure 12: Full scale numerical model illustrated by each layer
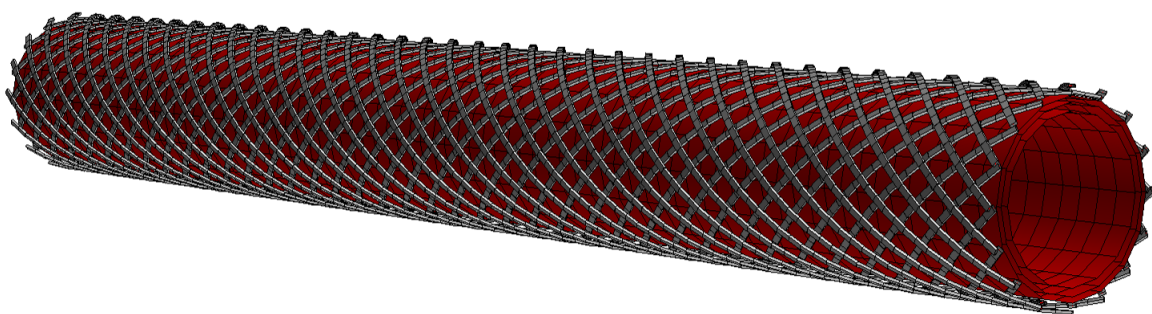
Figure 13: Full scale numerical model in a global view

24
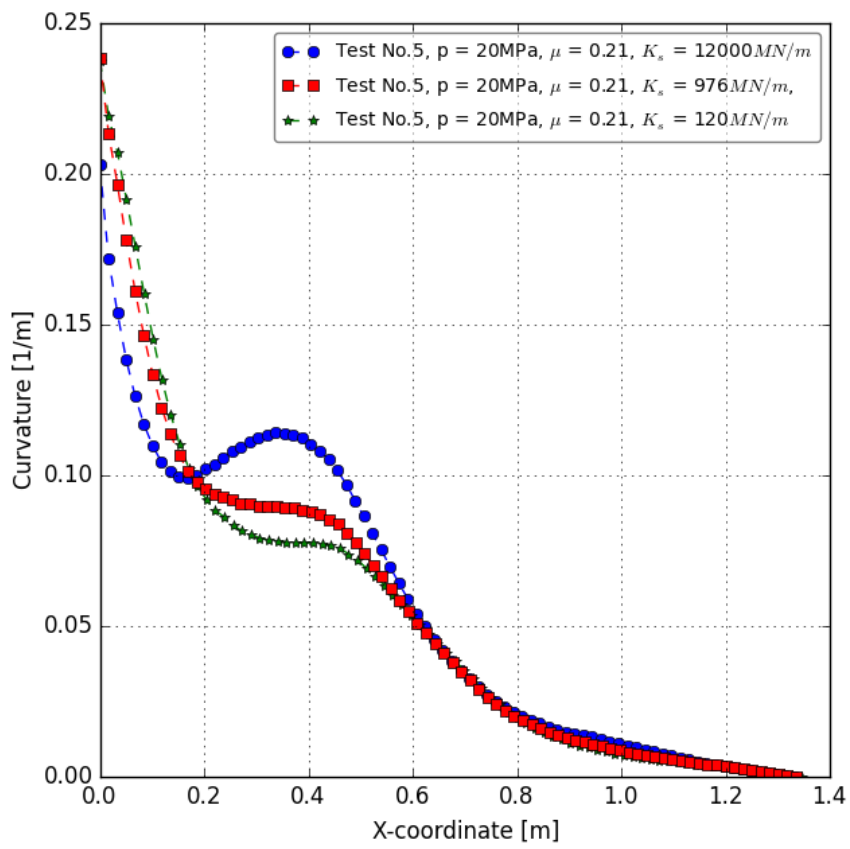
Figure 14: Spring stiffness effect on the curvature distribution along the model length by applying Coulomb friction model F_1
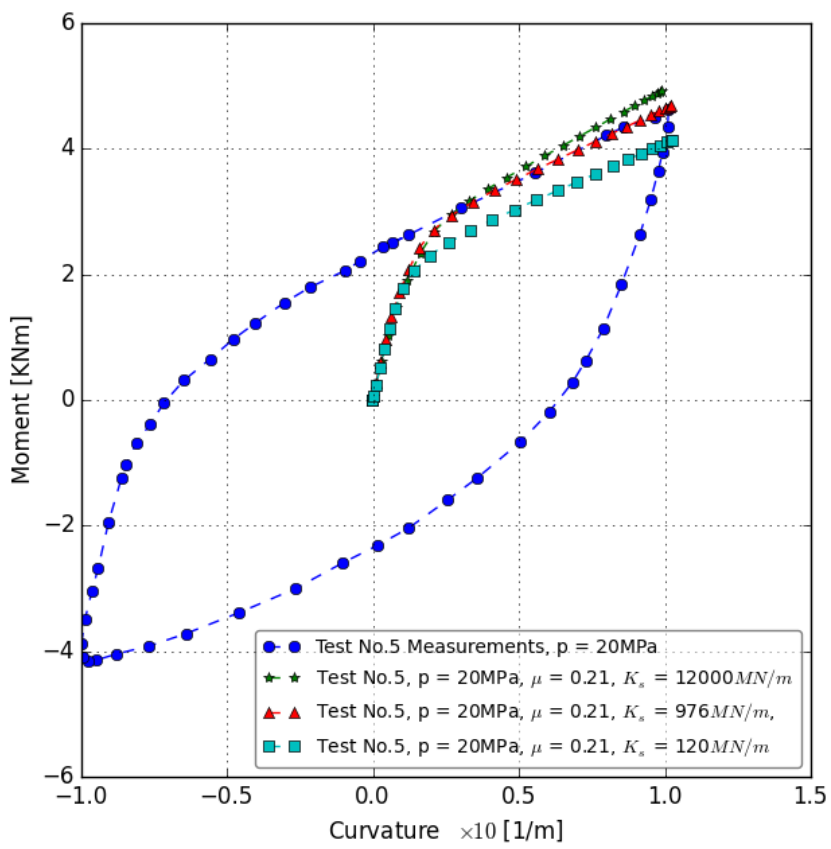
Figure 15: Spring stiffness effect on the bending moment-curvature behavior by applying Coulomb friction model F_1
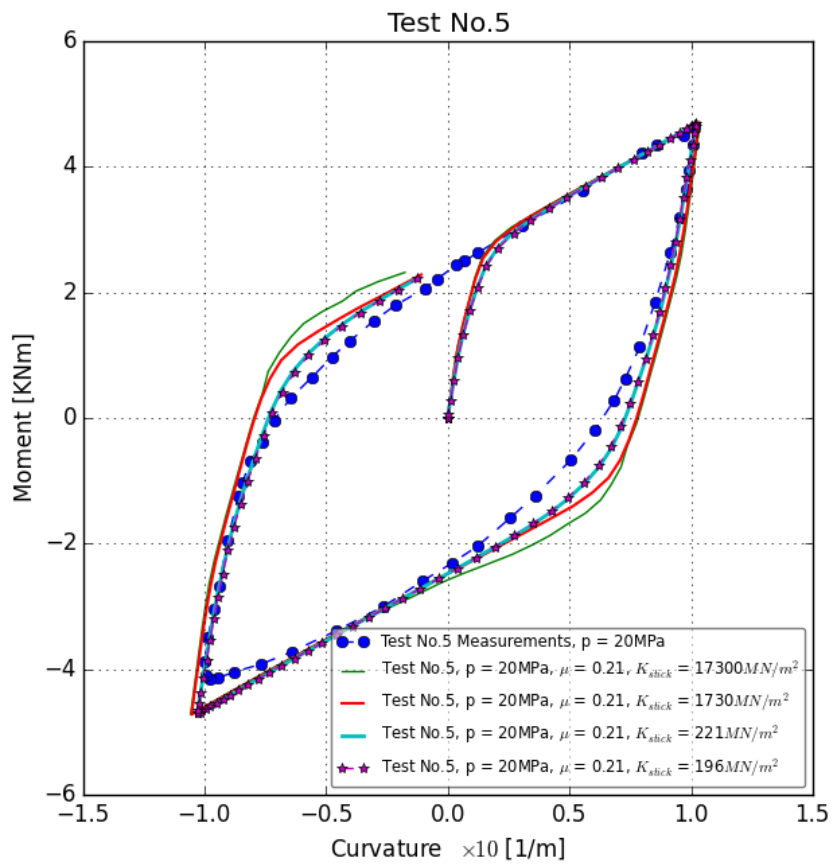
Figure 16: Sensitivity study of shear interaction stick stiffness by applying Coulomb friction model F_1
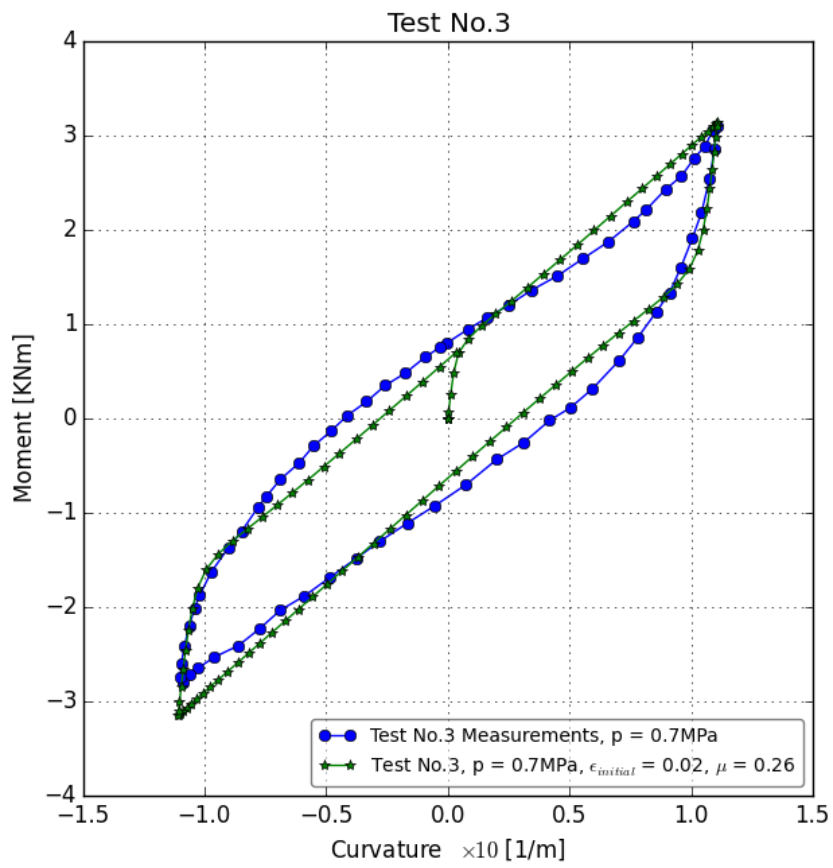
Figure 17: Correlation between Test No.3 measurements and numerical simulation results by applying Coulomb friction model F_1
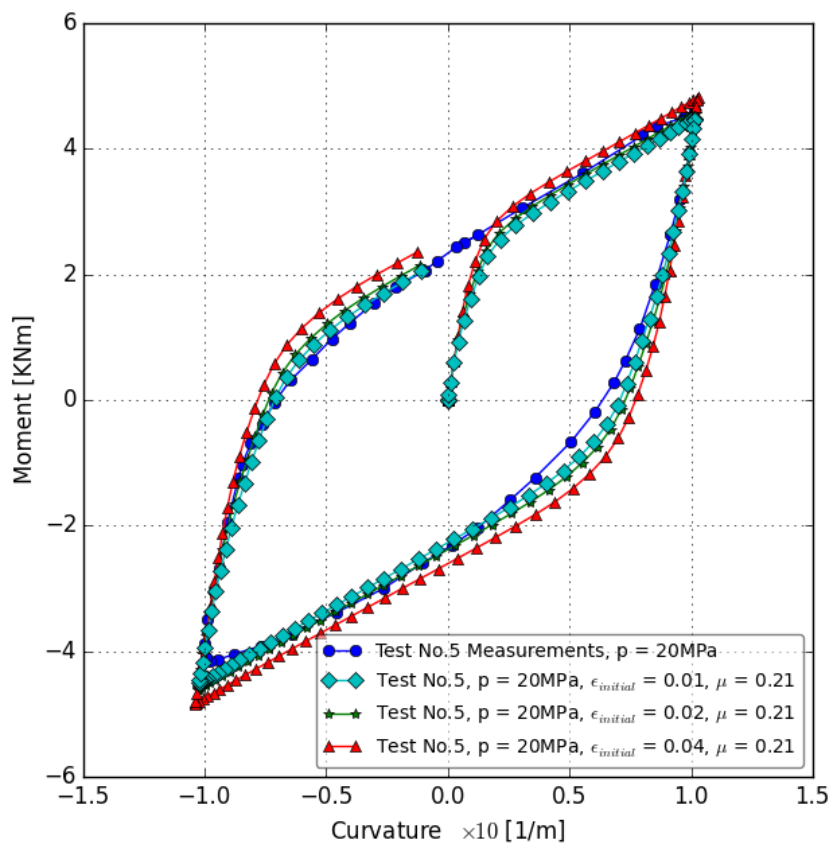
Figure 18: Sensitivity study of initial strain of outer sheath by applying Coulomb friction model F_1
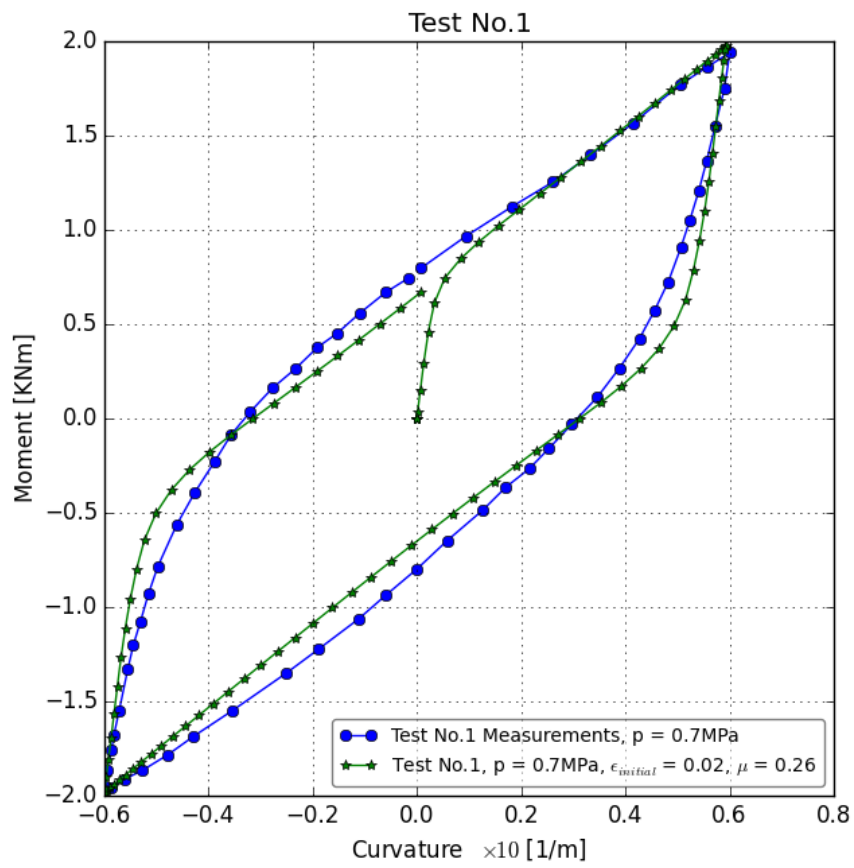
Figure 19: Correlation between Test No.1 measurements and numerical simulation results by applying Coulomb friction model F_1
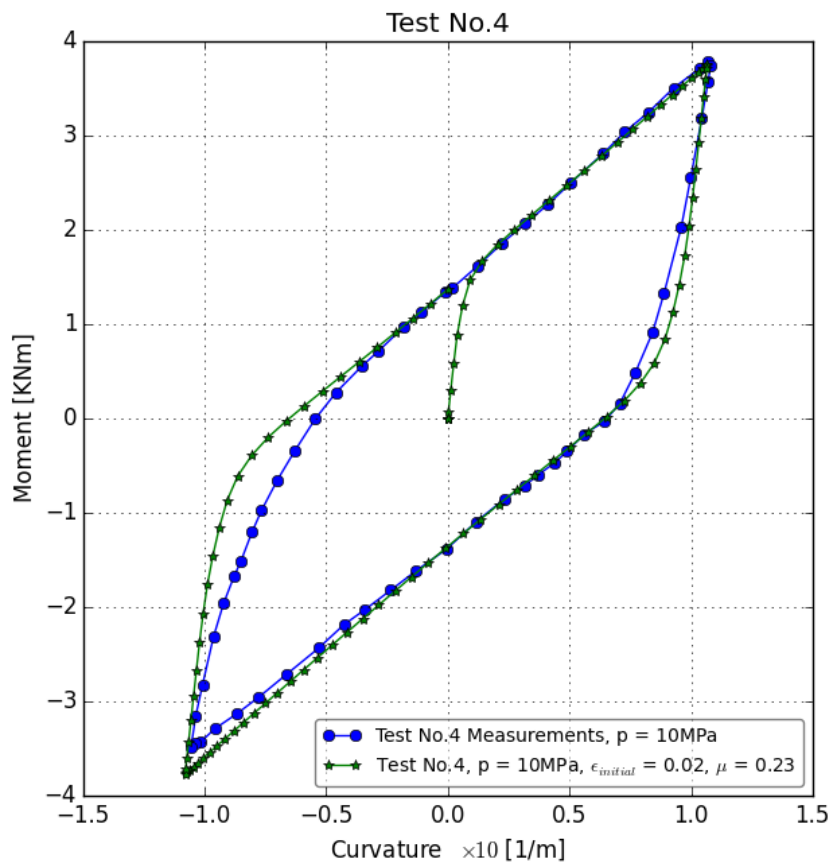
Figure 20: Correlation between Test No.4 measurements and numerical simulation results by applying Coulomb friction model F_1
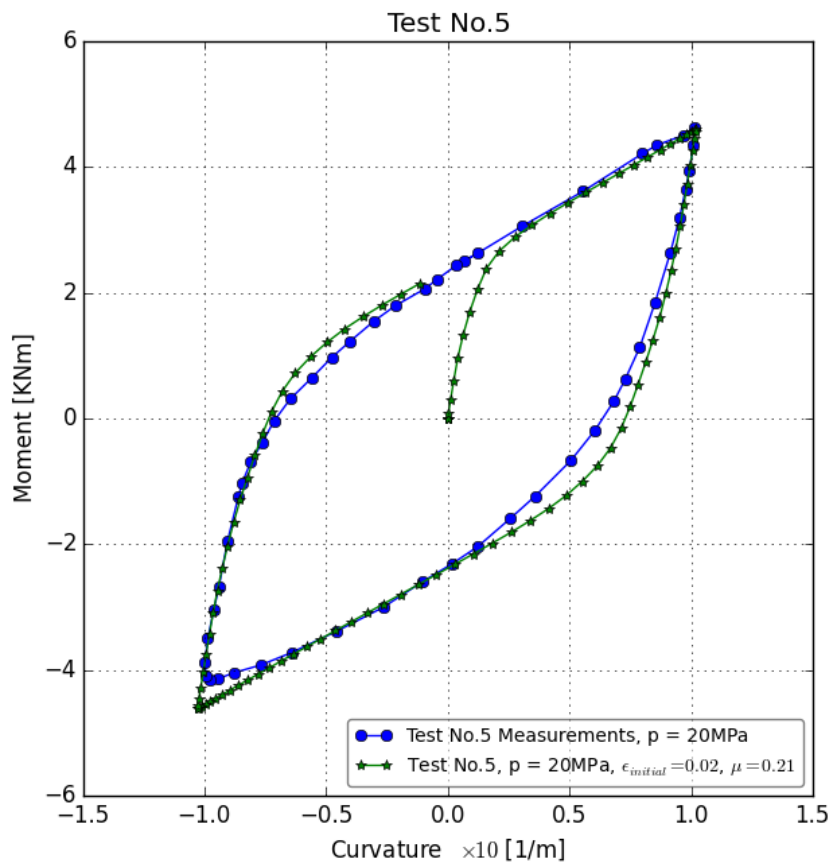
Figure 21: Correlation between Test No.5 measurements and numerical simulation results by applying Coulomb friction model F_1
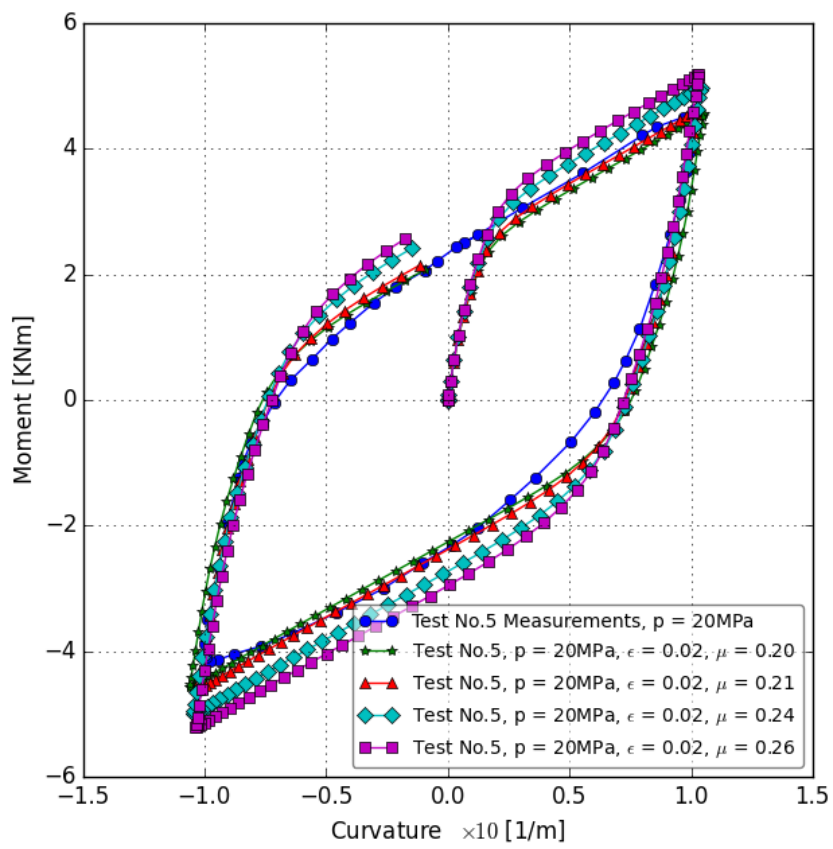
Figure 22: Sensitivity study of friction coefficient by applying Coulomb friction model F_1
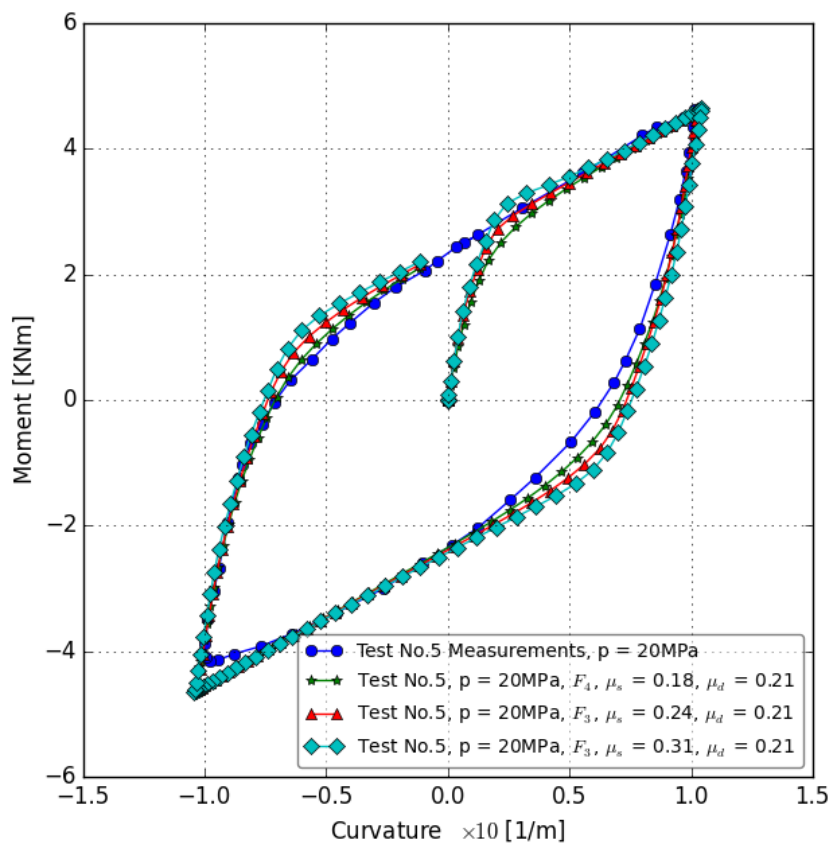
Figure 23: Friction models comparison

Reference

[1] Kavanagh WK, Gallagher K, Doynovand D, and Bai Y. The effect of tube friction on the fatigue life of steel tube umbilical risers-new approaches to evaluating fatigue life using enhanced nonlinear time domain methods. In *Offshore Technology Conference*. Offshore Technology Conference, 2004.

[2] Sødahl N, Skeie G, Steinkjer O, and Kalleklev A. Efficient fatigue analysis of helix elements in umbilicals and flexible risers. In *ASME 2010 29th International Conference on Ocean, Offshore and Arctic Engineering*, pages 1029–1037. American Society of Mechanical Engineers, 2010.

[3] Smith R, O'Brien P, O'Sullivan T, and Weibe C. Fatigue analysis of unbonded flexible risers with irregular seas and hysteresis. In *Offshore technology conference*. Offshore Technology Conference, 2007.

[4] Smith F, Grealishand R and Zimmermanand J. New industry guidelines for fatigue analysis of unbonded flexible risers. In *Offshore Technology Conference*. Offshore Technology Conference, 2006.

[5] Zhang Y, Chen B, Qiu L, Hill T, and Case M. State of the art analytical tools improve optimization of unbonded flexible pipes for deepwater environments. In *Offshore Technology Conference*. Offshore Technology Conference, 2003.

[6] Sævik S. Bflex theory manual. Marintek, 2010.

[7] Olsen E, Karlsen S, Jordal L, and Hansen-Zahl K. Determination of friction within a riser umbilical. In *ASME 2012 31st International Conference on Ocean, Offshore and Arctic Engineering*, pages 81–88. American Society of Mechanical Engineers, 2012.

[8] Rabinowiczt E. The nature of the static and kinetic coefficients of friction. *Journal of applied physics*, 22(11):1373–1379, 1951.

[9] Sævik S and Ekeberg KI. Non-linear stress analysis of complex umbilical cross-sections. In *ASME 2002 21st International Conference on Offshore Mechanics and Arctic Engineering*, pages 211–217. American Society of Mechanical Engineers, 2002.

[10] Sævik S. Theoretical and experimental studies of stresses in flexible pipes. *Computers & Structures*, 89(23):2273–2291, 2011.

[11] Ekeberg KI, Ottesen T, Aarstein J, Sævik S, Ye N, and Igland R. Predicting, measuring and implementing friction and bending stresses in dynamic umbilical design. In *Offshore Technology Conference*. Offshore Technology Conference, 2006.

[12] Andersen M, Berg A, and Sævik S. Development of an optical monitoring system for flexible risers. In *Offshore Technology Conference*. Offshore Technology Conference, 2001.

[13] Sævik S and Igland R. Calibration of a flexible pipe tensile armour stress model based on fibre optic monitoring. In *ASME 2002 21st International Conference on Offshore Mechanics and Arctic Engineering*, pages 53–58. American Society of Mechanical Engineers, 2002.

[14] Skallerud B. Structrual damping in wellstream pipe. In *Marintek*, 1991.

[15] Gaidai O, Ye N, Jin J, Reid D, and Mainçon P. Fatigue analysis methods of dynamic umbilicals. In *The Twenty fifth International Offshore and Polar Engineering Conference*. International Society of Offshore and Polar Engineers, 2015.

[16] Skallerud B. Damping models and structral damping in a nonbonded pipe. In *Marintek*, 1991.

[17] Ozaki S, Hikida K, and Hashiguchi K. Elastoplastic formulation for friction with orthotropic anisotropy and rotational hardening. *International Journal of Solids and Structures*, 49(3):648–657, 2012.

[18] Doynov K, Nilsen-Aas C, Haakonsen R, Wan K, and Bjærum R. Methodology for calculating irregular wave stress time histories of tensile wires in flexible risers. In *ASME 2007 26th International Conference on Offshore Mechanics and Arctic Engineering*, pages 91–101. American Society of Mechanical Engineers, 2007.

[19] Wang H, Ye N, Dai T, and Sævik S. Effect of surface contact stiffness on stress analysis of umbilicals. In *The Twenty-fifth International Offshore and Polar Engineering Conference*. International Society of Offshore and Polar Engineers, 2015.

[20] Feret J, J and Bournazel CL. Calculation of stresses and slip in structural layers of unbonded flexible pipes. *Journal of Offshore Mechanics and Arctic Engineering*, 109:263, 1987.

[21] Sævik S. On stresses and fatigue in flexible pipes. In *Ph.D Thesis*. Norwegian Institute of Technology, Trondheim, Norway, 1992.

[22] Sævik S and Li H. Shear interaction and transverse buckling of tensile armours in flexible pipes. In *ASME 2013 32nd International Conference on Ocean, Offshore and Arctic Engineering*. American Society of Mechanical Engineers, 2013.

[23] Litewka P. *Finite element analysis of beam-to-beam contact*, volume 53. Springer Science & Business Media, 2010.

[24] Hashiguchi K. Elastoplastic constitutive model with a subloading surface. In *Computational Mechanics 86*, pages 745–750. Springer, 1986.

[25] Hashiguchi K, Ozaku S, and Okayasu T. Unconventional friction theory based on the subloading surface concept. *International journal of solids and structures*, 42(5):1705–1727, 2005.

[26] Hashiguchi K and Ozaki S. Constitutive equation for friction with transition from static to kinetic friction and recovery of static friction. *International Journal of Plasticity*, 24(11):2102–2124, 2008.

[27] Sævik S. A finite element model for predicting stresses and slip in flexible pipe armouring tendons. *Computers & structures*, 46(2):219–23, 1993.

[28] Chang TY, Saleeb AF, and Shyu SC. Finite element solutions of two-dimensional contact problems based on a consistent mixed formulation. *Computers & structures*, 27(4):455–466, 1987.

[29] Sævik S and Ye N. *Aspects of design and analysis of offshore pipelines and flexibles*. Southwest Jiaotong University Press, 2016.

[30] Dunkin J and Kim E. Measurement of static friction coefficient between flat surfaces. *Wear*, 193(2):186–192, 1996.